Ni^{2+}/Co^{2+} doped Au-Fe_7S_8 nanoplatelets with exceptionally high oxygen evolution reaction activity

Shaghraf Javaid[a†], Xiaomin Xu[b†], Wei Chen[a], Jiayi Chen[a], Hsien-Yi Hsu[c,d], Sheng Wang[e], Xuyong Yang[e], Yunguo Li[f,*], Zongping Shao[b,*], Franca Jones[a,*], Guohua Jia[a,*]

[a]*School of Molecular and Life Sciences, Curtin University, Perth, WA 6102, Australia.*

[b]*WA School of Mines: Minerals, Energy and Chemical Engineering (WASM-MECE), Curtin University, Perth, WA 6102, Australia.*

[c]*School of Energy and Environment & Department of Materials Science and Engineering*

[d]*City University of Hong Kong, Kowloon Tong, Hong Kong, China*

Shenzhen Research Institute of City University of Hong Kong, Shenzhen 518057, China

[e]*Key Laboratory of Advanced Display and System Applications of Ministry of Education, Shanghai University, 149 Yanchang Road, Shanghai 200072, China*

[f]*CAS Key Laboratory of Crust-Mantle Materials and Environments, School of Earth and Space Sciences, University of Science and Technology of China, Hefei 230026, China.*

Corresponding authors:
E-mail: liyunguo@ustc.edu.cn; zongping.shao@curtin.edu.au; f.jones@curtin.edu.au; guohua.jia@curtin.edu.au

† These authors contributed equally to this work.

Abstract: To overcome the limited potency of energy devices such as alkaline water electrolyzers, the construction of active materials with dramatically enhanced oxygen evolution reaction (OER) performance is of great importance. Herein we developed an ion diffusion-induced doping strategy that is capable of producing Ni^{2+}/Co^{2+} doped two-dimensional (2D) Au-Fe_7S_8 nanoplatelets (NPLs) with exceptionally high oxygen evolution reaction (OER) activity outperforming the benchmark RuO_2 catalyst. The co-existence of Co and Ni in Au-Fe_7S_8 NPLs led to the lowest OER overpotential of 243 mV at 10 mA cm^{-2} and fast kinetics with Tafel slope of 43 mV dec^{-1}. Density functional theory (DFT) calculations demonstrated that Ni^{2+}/Co^{2+} doping improves the binding of OOH species on the {001} surfaces of Au-Fe_7S_8 NPLs and lowers the Gibbs free energy of the OER process, which are beneficial to outstanding OER activity of the nanoplatelets.

Graphical abstract

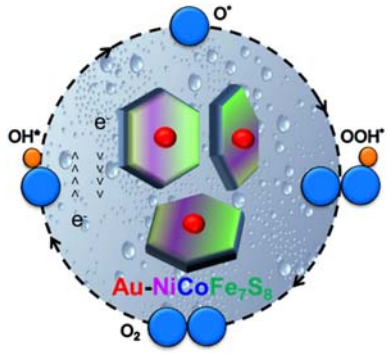

Keywords: oxygen evolution reaction, doping, nanoplatelets, Au-Fe_7S_8.

1. Introduction

Electrocatalytic water splitting is an efficient way to convert the renewable electrical energy into chemical fuel in the form of hydrogen and oxygen by means of hydrogen evolution reaction (HER) and oxygen evolution reaction (OER).[1-3] This process, which embodies two half reactions occurring at cathode and anode respectively, holds special significance due to its

ability to generate renewable energy for energy conversion and storage devices. The OER process, as compared to the HER, is restrained to a much greater extent by the slow kinetics, leading to a thermodynamic "*up-hill*".[4-7] In this regard, the access to stable and efficient electrocatalysts which can boost the kinetics and reduce the overpotential is of utmost importance. In light of the aforementioned issues, the formation, understanding and exploration of unique catalysts with well-defined structure and supreme performance in OER have become a hot pursuit.[8-12]

As emerging nanostructures with superior conductivity, transition metal chalcogenides have been in spot-light from last decade for energy-related reactions due to the relatively lower activation energy for the transfer of electron between cations.[13-19] Besides this, the presence of cations with multiple valencies imparts transition metal sulfides with desirable electrochemical features towards OER.[20, 21] This has been mainly ascribed to the ease in their compositional tuning for regulating the electronic and structural properties by means of doping and substitution. The elements of nickle and cobalt are just next to iron and they have similar radii while locating in the same row of the periodic table of elements. Doping Ni^{2+} and/or Co^{2+} could not only increase the composition diversity of iron compounds, but also improve their catalytic activities through modifying the electronic structures of the host materials using the dopants. A number of recent reports have suggested the significantly enhanced OER performance by employing binary and ternary nickel-iron-cobalt (Ni-Fe-Co) based electrocatalysts. For instance, loading of Fe_3O_4 into the Co_9S_8 NPs to produce Fe_3O_4@Co_9S_8/rGO-2[22] heterostructure leads to the increase in OER performance with an overpotential of 340 mV. This was credited to the ease in breaking the Co-O bond by virtue of electron transfer from Fe to Co_9S_8. Similarly, Zhan *et al.* [23] recently reported nanoarrays of sea-urchin like Fe doped FeNiCoP structure with an overpotential of 259 mV for OER, ascribed to synergistic effect and fast electron kinetics. Other examples include $NiFeS_2$[24], CoFeSP/CNT[25], P-$(Ni,Fe)_3S_2$/NF[26] nanostructures and so on. In spite of their improved performance, some of these reported

structures lag behind in terms of well-defined morphology while others in novel integration of Fe, Co and Ni chalcogenides in one system. Some additional challenges involve complex synthesis approach, big dimensions and obscurity around underpinning the exact mechanism for improved OER performance in Fe, Co and Ni hybrid catalyst.[27]

Multiple methods are available for the synthesis of hybridized structures of Fe, Co and Ni sulfides with an impressive variety in shapes and sizes on the grounds of their adjacent position in the periodic table.[10, 27-31] Among other doping methods, post-synthetic ion diffusion stands out the most.[32] Chen *et* al.[33] have reported this mechanism as a two-step process which begins with surface adsorption followed by lattice incorporation. By using performed host nanocrystals (NCs) all of the follow-up change in its properties can be entirely assigned to the dopant atoms which would be otherwise very complicated, if introduced during synthesis, to differentiate between the influence of dopant and its precursor on the host NCs.[34] It is noteworthy that the synergistic interaction of dopant atoms with the host material can switch p-type carriers of Fe into n-type by slightly altered electronic properties of Co[7, 33-37] and introduce sub-energy bands which in effect reduces the bandgap and henceforth overpotential.[8, 32, 38-40] In addition to the aforementioned reason, morphology and dimension of the final structure is also considered as one of the major factors in lowering the onset potentials for electrocatalytic water oxidation because of its direct link with stability, large surface area and availability of enough space for the diffusion of electroactive species.[29, 37-40]

However, as mentioned above, the intrinsic and extrinsic catalytic mechanisms in regards to the involved active sites are still under debate and are not well understood.[8, 9, 25, 26, 28-30] For instance, several studies claim that in Fe-Ni based catalysts, Fe^{III} acts as a Lewis acid and facilitates the formation of Ni^{IV} and Co^{III} which in turn act as the active sites.[37, 41] Other studies provided different perspectives that Ni/Co merely acts as conductive support to Fe active sites during OER or Fe and Ni/Co works collectively to boost the overall catalytic performance which essentially means that Fe^{IV} is as equally contributing as Ni^{IV} towards the OER process.[37,

[41-43] Further studies to elucidate how the addition of Ni/Co can enhance the performance of the catalysts and to reveal the underpinned mechanisms are highly desirable.

Semiconductor nanoplatelets are a type of intriguing materials that have attracted tremendous attention. They have giant oscillation strength and the charge carriers of nanoplatelets are generally confinement along their thickness direction,[44] thus providing an ideal model to couple the experimental and theoretical investigations on structure – performance relationship of nanomaterials. Nanoplatelets with such a unique shape offer more access to the active sites anchored on their surfaces and therefore maximizing the number of catalytic sites and areal density. Intrigued by these rationales, herein, we have selected two-dimensional (2D) Au-Fe_7S_8 nanoplatelets (NPLs) [45] as a host material which has valence states of both Fe^{II} and Fe^{III} for the synthesis of bi and trimetallic systems i.e. Ni^{2+}or Co^{2+} monodoped and Ni^{2+}/Co^{2+} co-doped systems and used Ni-doped, Co-doped, and Ni/Co-codoped Au-Fe_7S_8 nanoplatelets as the electrocatalysts for OER (Scheme 1). This particular form of iron sulfide, Fe_7S_8, offers an advantage of providing mixed valence states and crystal defects which are believed to originate from sulfur vacancies.[8] A facile approach of ion diffusion was developed to prepare Co and Ni doped Au-Fe_7S_8 NPLs while still retaining its 2D hexagonal morphology (Scheme 1). To investigate the effect of multimetals towards electrocatalysis, Co and Ni dopants were introduced both individually and collectively to develop three different heterostructures i.e. Au-Co/Fe_7S_8, Au-Ni/Fe_7S_8 and Au-NiCoFe_7S_8. The as-prepared NPLs exhibited drastically improved and remarkable OER activity that outperformed the benchmark RuO_2 catalyst. Such substantial improvement in electrocatalytic performance is attributed to the modified electronic structure as demonstrated by DFT calculations where Co and Ni doping induces lowering of the Gibbs-free energy at an active site of Fe (001). The interaction between Fe, Co and Ni constituent metals, i.e. the synergy between active centres and ease in ion diffusion leading to gas release is an additional contributing factor.

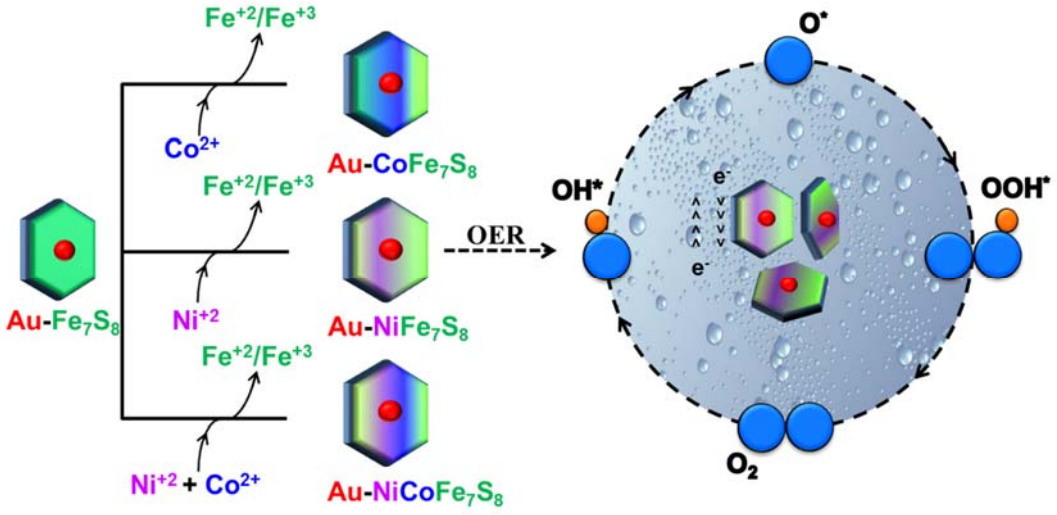

Scheme 1. Schematic illustration of doping of Co, Ni and NiCo performed on Au-Fe_7S_8 and proposed mechanism for OER.

2. Results and discussion

The synthesis route of Ni and Co doped Au-Fe_7S_8 NPLs is schematically illustrated in Scheme 1, where one-step post synthetic modification approach was used (see experimental section for further details). First, 2D Au-Fe_7S_8 NPLs were fabricated (Figure S1) by our previously reported seeded growth method [45] and particular attention was paid to the washing of these NPLs in order to get rid of any unreacted precursor and impurities. In the next step, the obtained Au-Fe_7S_8 NPLs were further subjected to modification by means of individual and simultaneous doping of Ni and Co ion at 200 °C for 3 hrs to finally produce three unique and exclusive 2D NPLs with hexagonal morphology, i.e., Au-$CoFe_7S_8$, Au-$NiFe_7S_8$ and Au-$NiCoFe_7S_8$, as demonstrated in scheme 1.

It should be noted here that the precursor ratios and other experimental parameters were adjusted in such a way that ensured only controlled diffusion of Co and Ni ions into the starting Au-Fe_7S_8 NPLs rather than nucleating separately. Electron microscopic investigations (Figure 1) were performed to understand the influence of ion diffusion (Co and Ni) on the size, morphology and composition of Au-Fe_7S_8 NPLs with the advent of chemical reaction. All three

ion diffusion products retained hexagonal morphology, Au seed in the centre and two-dimensionality as demonstrated in Figure 1, where NPLs standing on its edges are quite obvious. The statistical analysis on the size distribution of all three reported NPLs, Au-$CoFe_7S_8$, Au-$NiFe_7S_8$ and Au-$NiCoFe_7S_8$ NPLs (Figures S2-S4) shows that their diameter is in the range of 76-82 nm respectively which is slightly higher than the starting Au-Fe_7S_8 NPLs, i.e., around 69 nm. The increase in diameter can be attributed to the diffusion of Co and Ni metal ions into the defect-rich Fe_7S_8 lattices.[46]

Figure 1a1-c1 presents the high angle annular dark field-scanning transmission electron microscopy (HAADF-STEM) images of Au-$CoFe_7S_8$, Au-$NiFe_7S_8$ and Au-$NiCoFe_7S_8$ with their corresponding TEM and high-resolution TEM (HRTEM) images given in Figure 1a2-c2 and a3-c3, respectively. Figure 1a3-c3 is the classic demonstration of the dimension of an isolated particle with a closer view and high crystallinity with distinct spots in Fast Fourier Transform (FFT) pattern (inset) which were analogous to the main NPLs constituent, i.e., Fe_7S_8.[45] Similar interplanar distances of 2.97 and 1.71Å were dominant in the pristine Au-Fe_7S_8 NPLs corresponding to the $(\bar{1}22)$ and (040) lattice planes, respectively. The superimposition of $(\bar{1}22)$, (040) and (320) planes in Figure 1a3, b3 just reflects that there is a second crystal within the selected area. The 2D repeating pattern of spots comes from the flat plate which appears to be a single crystal. The fact that the additional spots are just a single pair of spots with no apparent angular relationship to the underlying hexagonal pattern suggests there is no crystallographic relationship between the plate and the extra bit of crystalline material. Here it is important to emphasize that no additional phases in relation to CoS and NiS or the mixture of their alloys were observed during the structural analysis of the TEM images. This means that the ion diffusion of Co^{2+} and Ni^{2+} during the post-synthetic procedures does not alter the lattice structures of the original Fe_7S_8 NPLs. This initial outcome was picked up as a clue that this process is most likely a diffusion induced doping process instead of ion displacement or cation exchange.

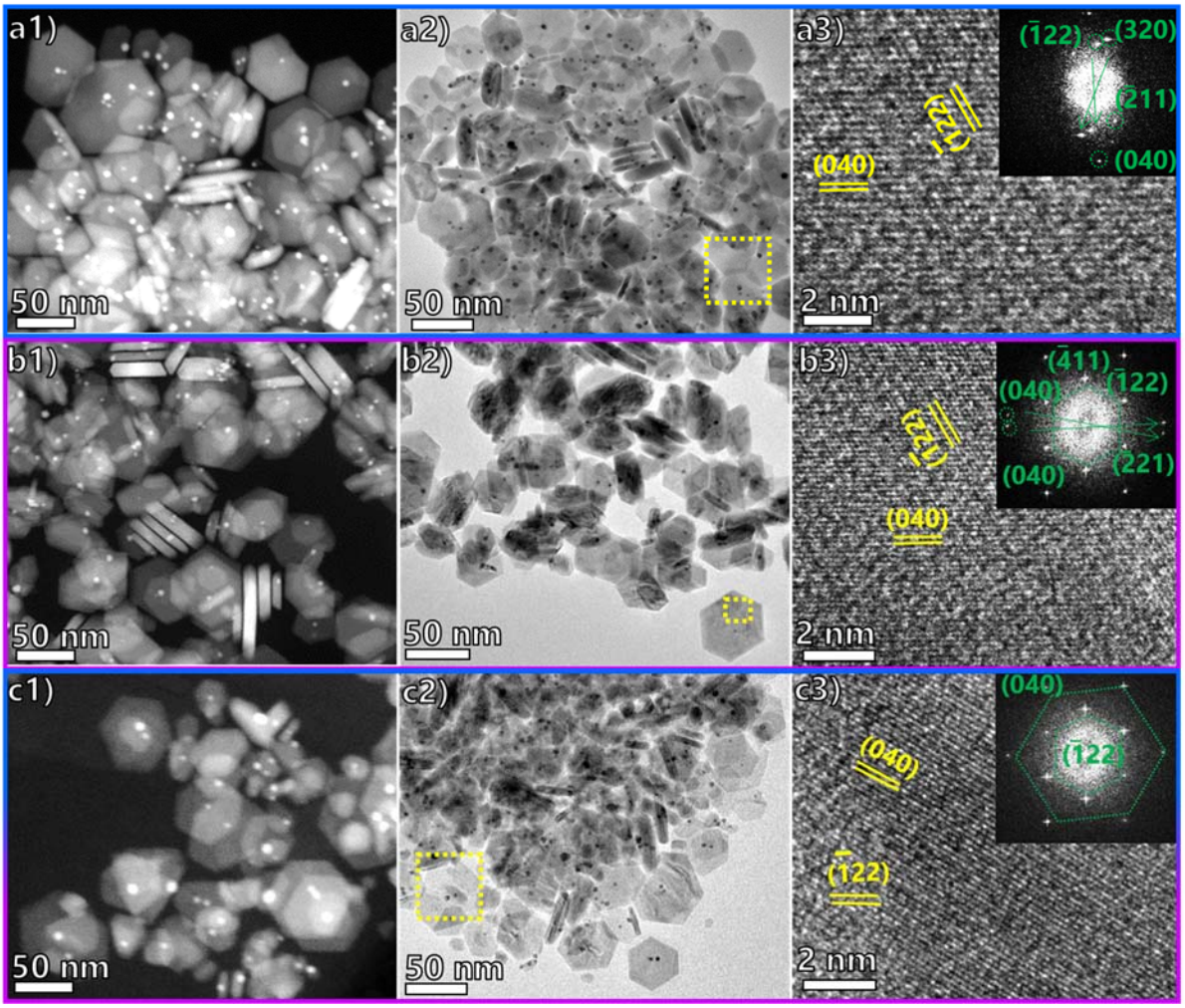

Figure 1. Representative STEM, TEM, HRTEM images and corresponding FFT patterns of (a1-a3) Au-$CoFe_7S_8$, (b1-b3) Au-$NiFe_7S_8$ and (c1-c3) Au-$NiCoFe_7S_8$ respectively. Yellow rectangles show the respective areas where HRTEM analysis was performed.

To verify the claimed parameters as optimum experimental conditions, another parallel experiment was carried out on Au-$NiCoFe_7S_8$ NPLs where precursor ratio of Ni/Co was doubled as compared to Fe in pristine Au-Fe_7S_8 NPLs. Theoretically, it should have increased the rate of diffusion to produce an entirely new hybrid heterostructure of Au-NiCoS. Instead, substantial amounts of homogeneous nucleation was observed (Figure S5) which was linked to the reaction equilibrium and thermodynamic limits. This set of data strengthens the importance of optimum conditions required to achieve controlled diffusion, as observed in Figure 3.

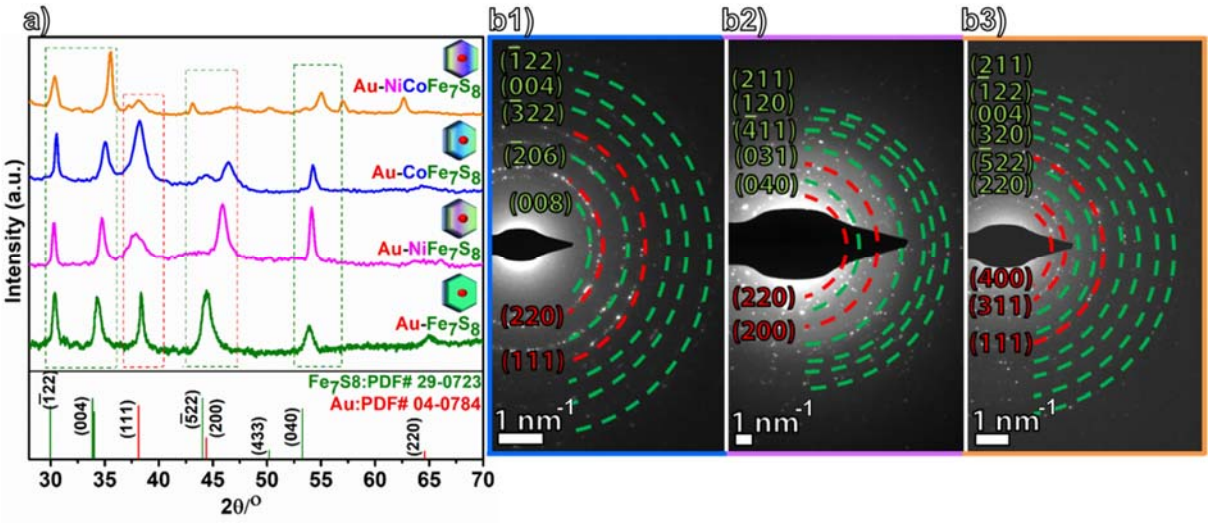

Figure 2. Structural characterization of ternary hybrid NPLs. (a) XRD pattern of Au-Fe_7S_8, Au-$NiFe_7S_8$, Au-$CoFe_7S_8$ and Au-$NiCoFe_7S_8$. (b1-b3) SAED pattern of Au-$CoFe_7S_8$, Au-$NiFe_7S_8$ and Au-$NiCoFe_7S_8$ respectively.

The XRD patterns (Figure 2a) of both doped and undoped samples primarily exhibit two sets of diffraction peaks which matched well with the face centred cubic Au (JCPDF#04-0784) and monoclinic Fe_7S_8 (JCPDF#29-0723), respectively.[45-48] However, notably a diffraction shift of around 1° was observed in the XRD spectra of Au-$NiCoFe_7S_8$. The reason behind this shift was attributed to the change in cell dimension (lattice parameters) and therefore residual crystal strain. The prominent display of this shift only in Au-$NiCoFe_7S_8$ NPLs could be ascribed to the slight atomic radius change due to simultaneous doping of Ni^{2+} and Co^{2+} into the Fe_7S_8 crystal lattice. For the same catalyst, Au-$NiCoFe_7S_8$, even with repeated tailoring of experimental parameters, some homogeneous nucleation of nickel and cobalt sulfide with irregular morphology was observed (Figure S6), which clearly explain the existence of the additional XRD peaks in the sample of Au-$NiCoFe_7S_8$ NPLs. This claim was further supported by collecting selected-area electron diffraction (SAED) pattern of Au-$CoFe_7S_8$, Au-$NiFe_7S_8$ and Au-$NiCoFe_7S_8$ NPLs (Figure 2b1-b3). When assigned, the rings of diffraction spots were in close agreement with pristine Au-Fe_7S_8 NPLs,[45] designated in red and green colour, respectively. The overlapping of prominent *hkl* values indexed to the $(\bar{1}22)$ and (040) planes in

FFT, XRD and SAED endorses the correct assignment of the Au and Fe_7S_8 which anneals the formation of ion diffusion products.

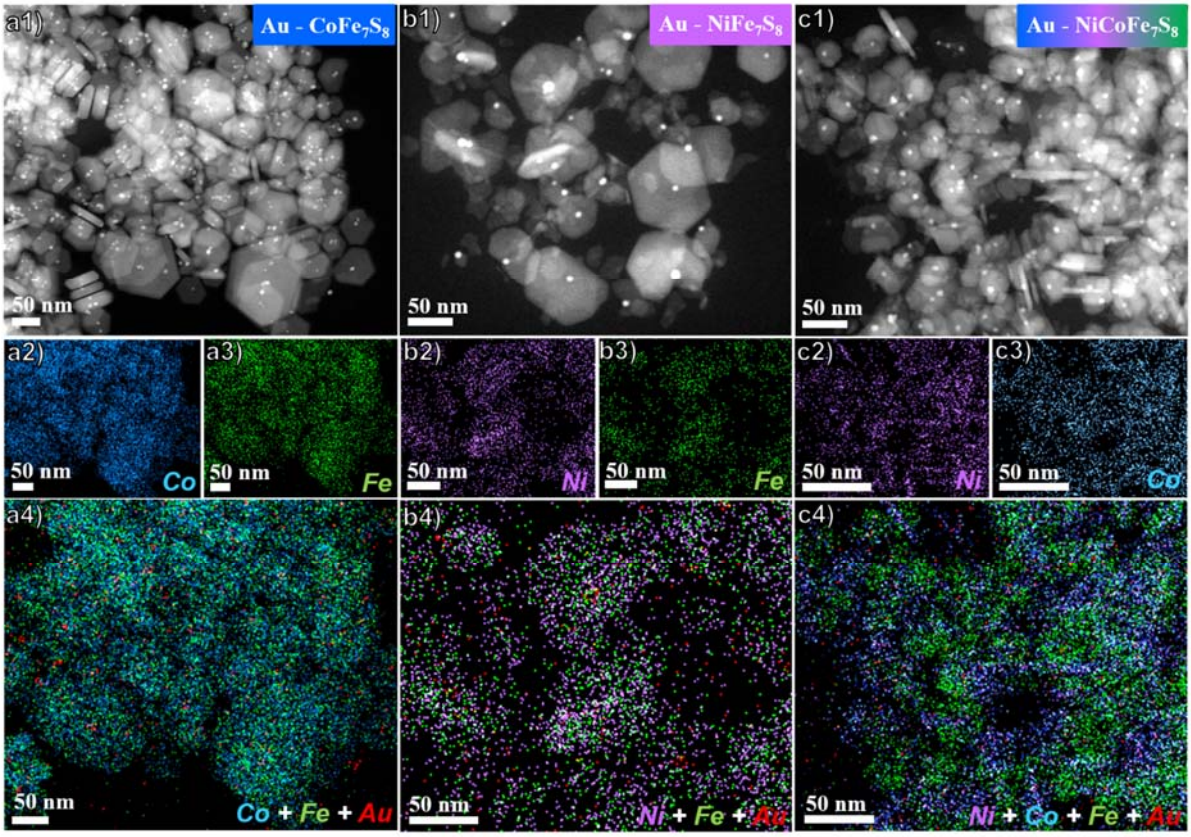

Figure 3. HAAD-STEM images and EDS mapping showing the distinct locations of Fe, Co and Ni and constituents (a1-a4) Au-$CoFe_7S_8$ (b1-b4) Au-$NiFe_7S_8$, (c1-c4) Au-$NiCoFe_7S_8$, respectively.

To determine the location, atomic arrangement and most importantly the co-existence of the three integral components (Fe, Co, Ni) of the synthesized NPLs, HAADF-STEM analysis was performed (Figure 3). It was used to construct the STEM-EDS elemental maps of all three doped Au-$CoFe_7S_8$, Au-$NiFe_7S_8$ and Au-$NiCoFe_7S_8$ NPLs as shown in the bottom panel of Figure 4a1-c4 with their corresponding EDS spectra (Figures S7-S9). The homogeneous distribution of Co and Ni suggests their uniform incorporation into the Au-Fe_7S_8 NPLs rather than forming any localized domains. These maps not only confirm the retention of the original

constituents of the NPLs but also the distribution of Co and Ni within the Fe_7S_8 lattice throughout the particle.

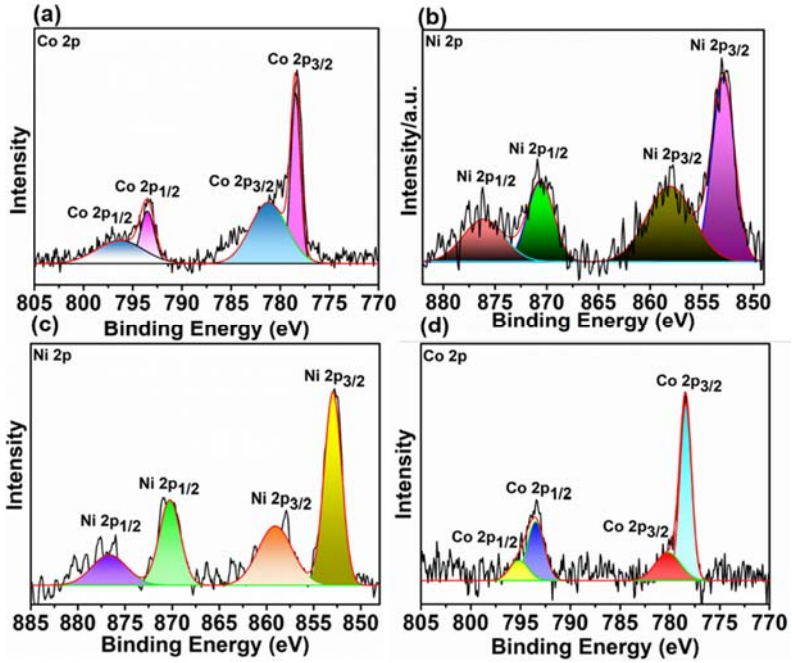

Figure 4. High resolution XPS spectra of (a) Co (b) Ni and (c and d) Co, Ni for Au-$CoFe_7S_8$, Au-$NiFe_7S_8$, and Au-$NiCoFe_7S_8$, respectively.

To analyse the surface chemical composition, valence states, chemical constituents and their bonding environment, X-ray photoelectron spectroscopy (XPS) analysis was performed which confirmed the successful integration of Co and Ni into the as-synthesized NPLs. Figures S10-S12 depict the survey spectra of Au-$CoFe_7S_8$, Au-$NiFe_7S_8$ and Au-$NiCoFe_7S_8$ NPLs confirming the co-existence of Fe with Co and Ni. To illustrate the existence of introduced dopants, the high resolution XPS spectra of Co_{2p} in Au-$CoFe_7S_8$, Ni_{2p} in Au-$NiFe_7S_8$ and Co_{2p} and Ni_{2p} in Au-$NiCoFe_7S_8$ are presented in Figure 4a-4d, respectively. The Co 2p spectrum (Figure 4a) showed best fit for deconvoluted two spin orbits doublet at binding energies of 778.2, 781.2 and 793.4 eV, 796.3 eV assigned to Co $2p_{3/2}$ and Co $2p_{1/2}$, respectively while indicating the existence of Co^{2+}/Co^{+3} in Au-$CoFe_7S_8$.[49-51] Similarly, The Ni 2p spectrum (Figure 4b) was deconvoluted into two spin orbit doublets assigned to Ni $2p_{3/2}$ at Ni $2p_{1/2}$. The first doublet at 852.9 and 870.6 eV, and the second doublet at 858 and 876.2 eV advocates the

presence of both Ni^{+2} and Ni^{+3} in the Au-$NiFe_7S_8$ NPLs.[3, 51, 52] Almost identical results were observed for both Co and Ni in Au-$NiCoFe_7S_8$ as shown in Figure 4c-d. The detailed XPS investigations for pristine Au-Fe_7S_8 NPLs can be found in our previously published article.[45] A closed inspection on the O 1s XPS spectroscopy of the Au-$CoFe_7S_8$, Au-$NiFe_7S_8$ and Au-$NiCoFe_7S_8$ NPLs (Figure S13) showed the presence of only absorbed hydroxide ions attributed to moisture absorption.[53] The structure of as-prepared Au-Fe_7S_8, Au-$CoFe_7S_8$, Au-$NiFe_7S_8$ and Au-$NiCoFe_7S_8$ NPLs was further studied by Raman spectra (Figure S14). The prominent peaks in the range of 300 to 800 cm^{-1} were allocated to asymmetric Fe–S, Ni–S and Co–S stretching.[37, 54-56] Notably, the vibration energy of metal-S progressively shifts to high wavenumbers (cm^{-1}), which is consistent with the ascending order of the atomic number of Fe, Co and Ni. Based on the above analysis, it can be regarded as certain that the conversion of pristine Au-Fe_7S_8 to Au-$CoFe_7S_8$, Au-$NiFe_7S_8$ and Au-$NiCoFe_7S_8$ occurred via a simple single-step process. Based on the above analysis, it can be regarded as certain that the conversion of pristine Au-Fe_7S_8 to Au-$CoFe_7S_8$, Au-$NiFe_7S_8$ and Au-$NiCoFe_7S_8$ occurred *via* a simple single-step process.

The high demand of iron, cobalt and nickel sulfides in energy storage applications makes these platelets an interesting candidate for further exploration. It can be attributed to its multifunctionality due to the presence of dichalcogenides in a single particle.[3, 8, 9, 29, 31, 51] In light of this, the electrocatalytic performance of all three synthesized NPLs were evaluated towards the OER.

The electrocatalytic OER performance of the prepared samples was tested in oxygen-saturated 1.0 M KOH alkaline solution using a three-electrode configuration. Figure 5a shows the kinetic OER currents which were obtained by averaging the forward- and backward-going cyclic voltammetry scans, followed by compensation for electrolyte resistance (see Figure S15, Supporting Information, for an exemplary data processing). The pristine Au-Fe_7S_8 sample exhibited a negligible current response across the potential range of 1.2−1.7 V vs. the reversible hydrogen electrode (RHE), indicative of its poor catalytic activity toward the OER. By stark

contrast, Au-$CoFe_7S_8$, Au-$NiFe_7S_8$, and Au-$NiCoFe_7S_8$ showed a much earlier onset for initiating the OER currents (i.e., at potentials even lower than 1.55 V), suggesting the drastically enhanced OER kinetics upon the incorporation of Co or/and Ni. When one compares the overpotential needed to reach an OER current density of 10 mA cm^{-2} (η_{10}), a metric commonly used for OER activity comparison due to its close relation to solar fuels production [57], Au-$NiCoFe_7S_8$ was found to give the lowest value of 243 mV, followed by Au-$NiFe_7S_8$ (259 mV) and Au-$CoFe_7S_8$ (275 mV) (Figure 6a inset). Of note, these η_{10} values are much smaller than that found on the benchmark RuO_2 catalyst (368 mV, consistent with previous reports[22]), which highlights the high efficacy of these doped iron sulfide materials for electrocatalyzing the OER. More importantly, to deliver a current density as high as 100 mA cm^{-2}, the co-doped sample only required an overpotential of less than 300 mV (i.e., 288 mV), lower than that of the Ni- and Co-doped counterparts (306 and 324 mV, respectively).

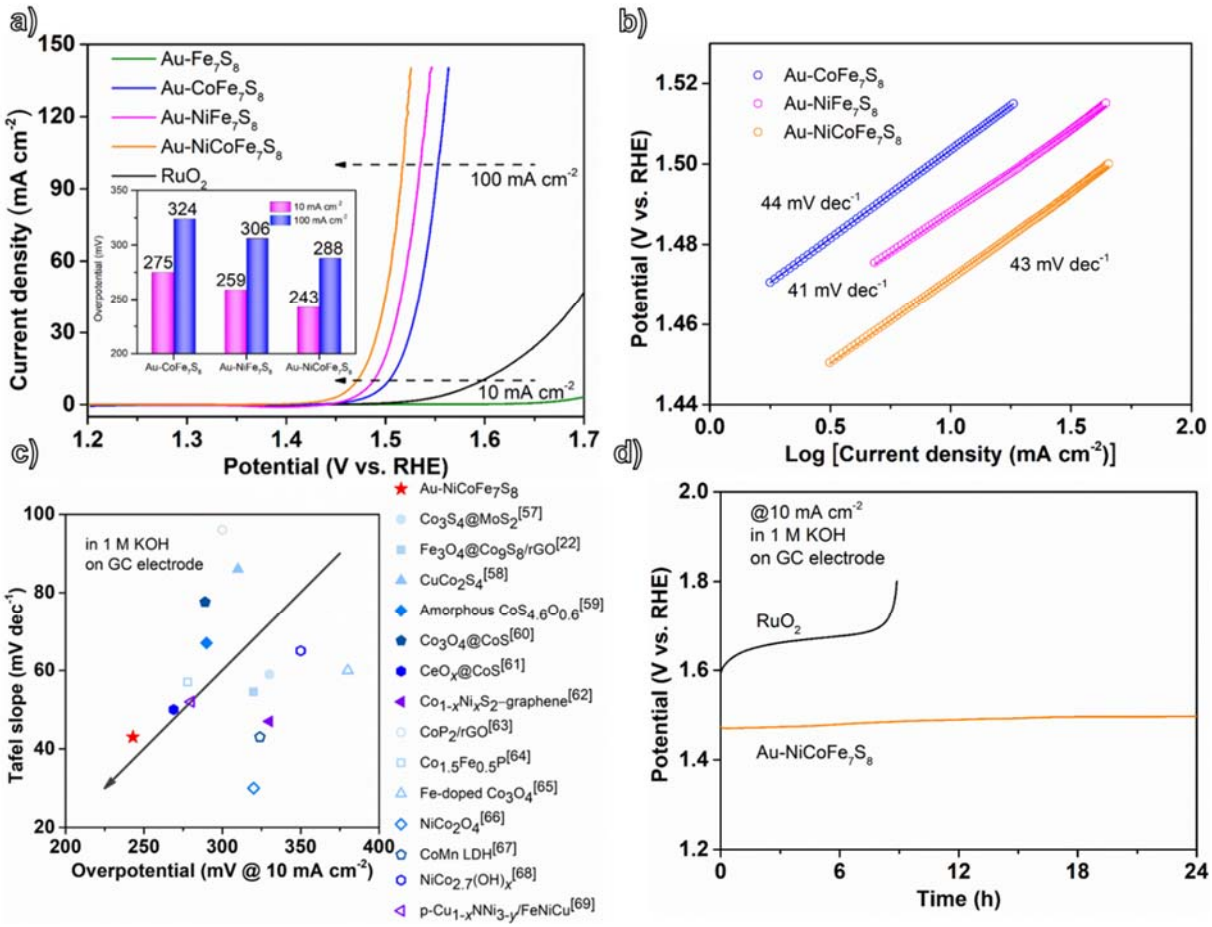

Figure 5. Electrocatalytic OER performance of Au-$NiCoFe_7S_8$. (a) OER kinetic currents of Au-Fe_7S_8, Au-$CoFe_7S_8$, Au-$NiFe_7S_8$, Au-$NiCoFe_7S_8$, and RuO_2 in 1 M KOH solution. Inset shows a comparison of the overpotential needed to reach 10 and 100 mA cm^{-2}. (b) Tafel plots of Au-$CoFe_7S_8$, Au-$NiFe_7S_8$, and Au-$NiCoFe_7S_8$. (c) A comparison of the OER activity of Au-$NiCoFe_7S_8$ with other reported state-of-the-art catalysts tested on GC electrode in 1 M KOH electrolyte, using the overpotential needed to reach 10 mA cm^{-2} and Tafel slope. Solid symbols represent sulfide-based catalysts and hollow symbols represent other types of catalysts.[22, 57-69] (d) Chronopotentiometry curves of Au-$NiCoFe_7S_8$ and RuO_2 at a constant current density of 10 mA cm^{-2}.

These results suggest that the co-doping of Co and Ni could lead to a greater activity increase as compared with the mono-doping of Co or Ni. Because these samples have a similar platelet size (Figure S1), such activity difference is more likely associated with their intrinsic materials properties than any difference in the surface areas, which will be discussed in more detail in the DFT section. The excellence of these doped sulfide samples was further demonstrated by means of the Tafel plots. As shown in Figure 5b, all the doped samples had Tafel slopes in the range of 41−43 mV dec^{-1}, much smaller than those of Au-Fe_7S_8 (73 mV dec^{-1}) and RuO_2 (69 mV dec^{-1}) (Figure S16, Supporting Information), again showcasing the impressively accelerated OER kinetics on the doped samples. The observation of the similar Tafel slopes suggests that the doped iron sulfide samples may catalyze the OER by using the same reaction mechanism. Having both low overpotential and low Tafel slope, the co-doped Au-$NiCoFe_7S_8$ catalyst ranks among the best-performing, non-noble metal-based OER catalysts reported to date, as seen from a detailed comparison with catalysts ranging from sulfide-based materials and beyond (e.g., phosphide, oxide, nitride, and hydroxide) (Figure 5c and Table S1, Supporting Information). Notably, when carbon paper was adopted as the substrate in place of the glassy carbon (GC) electrode to allow for increased loading of catalyst, the overpotential could be further reduced (η_{10}=230 mV) while the fast reaction kinetics remains unaffected (Tafel slope: 43 mV dec^{-1}), as shown in Figure S17. Such small overpotential and

Tafel slope of the ternary Au-NiCoFe_7S_8 can be beneficial for practical electrochemical devices. It is worth mentioning here that Chen *et al*.[37] recorded the overpotential of 270 mV and Tafel slope of 43 $mVdec^{-1}$ from ultrathin (~1.78 nm) Fe_7S_8 nanosheets which suggest that by controlling the thickness of Au-NiCoFe_7S_8 catalyst, further enhancement in the OER performance can be expected. During the synthesis of pristine Au-Fe_7S_8 NPLs, Au NPs played a central role for the controlled growth of hexagonal shaped domain of Fe_7S_8 around it. These thiol (–SH) functionalized Au NPs operated as the seeds which were consequently seen embedded in the centre of Au-Fe_7S_8 NPLs.[45] Dimension and configuration are believed to have direct impact on the performance of multi-component materials and therefore remained one of the primary objective in the reported work. To reveal the importance of the morphology of the samples in OER catalytic activity, we synthesized Ni/Co doped Au-Fe_7S_8 nanoparticles that have irregular shape (Figure S18a). To reveal the importance of the morphology of the samples in OER catalytic activity, we synthesized Ni/Co doped Au-Fe_7S_8 nanoparticles that have an irregular shape (Figure S18a). Comparison of the OER activity of Ni/Co doped Au-Fe_7S_8 nanoparticles with an irregular shape with that of Ni/Co doped Au- Fe_7S_8 NPLs indeed shows that the increased OER catalytic performance of the NPLs sample compared to the sample with an irregular shape (Figure S18b), which confirms the importance of the nanoplatelet morphology toward enhanced OER catalysis. It should be stressed here, that the role of Au NPs was only restricted towards the morphology regulation and did not have any notable contribution towards the OER catalytic activity (Figure S19). The Au sample gave an OER current density of 3.46 mA cm^{-2} at a potential of 1.80 V vs. RHE, comparable to previously reported Au-based catalysts.[70, 71] Of note, such activity is negligible when compared to the Au-Fe_7S_8, Au-CoFe_7S_8, Au-NiFe_7S_8, and Au-NiCoFe_7S_8 samples, suggesting that Au in these sulfide-based catalysts contributes insignificantly to the OER catalytic activity.

To evaluate the electrochemical stability of Au-NiCoFe_7S_8, we first conducted continuous CV cycling at a slow scan rate of 10 mV s^{-1}. As presented in Figure S20, the pristine Au-Fe_7S_8

sample exhibited larger η_{10} values with the increase of cycle number, indicative of its poor catalytic stability. By comparison, Au-NiCoFe$_7$S$_8$ showed good electrochemical stability with no obvious increase in the η_{10} over the cycling test. The good stability of Au-NiCoFe$_7$S$_8$ was also verified by chronopotentiometry measurements. As depicted in Figure 5d, Au-NiCoFe$_7$S$_8$ maintained its activity when held at a constant current density of 10 mA cm^{-2} for 10 hours, whereas the RuO_2 standard gradually lost its activity during the same testing, due likely to the formation of soluble RuO_4^{2-} species under OER conditions[72]. Similarly, good catalytic durability was also found for the carbon paper supported Au-NiCoFe$_7$S$_8$ catalyst (Figure S21).

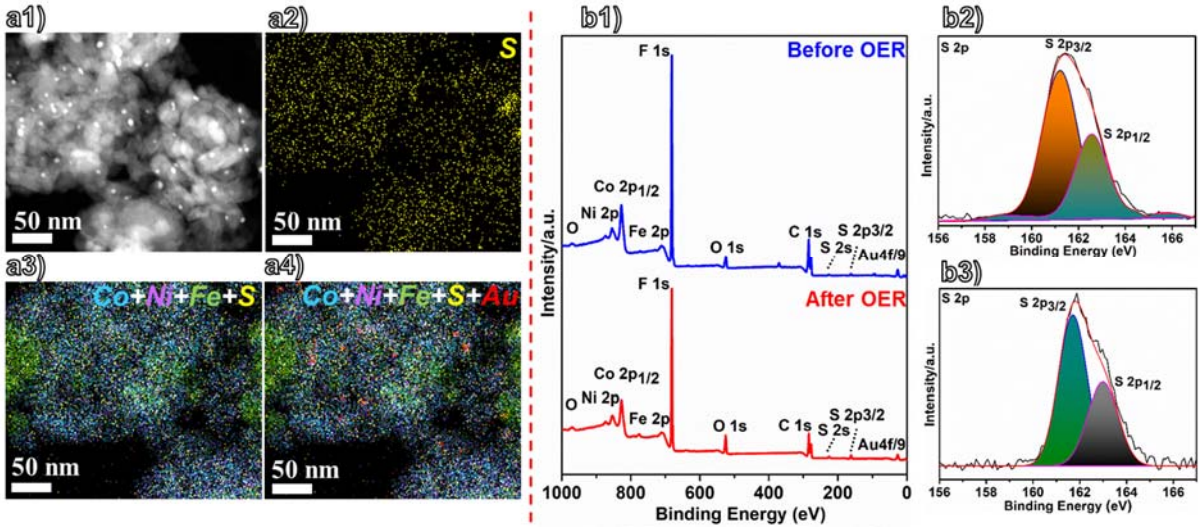

Figure 6. Characterizations of Au-NiCoFe$_7$S$_8$ NPLs after OER measurements. (a1-a4) STEM image, elemental maps (b1) XPS survey spectra, high resolution XPS spectra of S_{2p} (b2) before and (b3) after OER measurements.

Some further characterizations were performed to gain insights into the preservation of morphology and elemental content of the reported NPLs after being exposed under OER environment for extended period of time. For this purpose, only Au-NiCoFe$_7$S$_8$ NPLs were selected based on its outstanding performance and having both dopant entities i.e. Co and Ni. Figure 6a1-a4 illustrate the STEM images and elemental maps of the constituent entities after OER measurement for 12 hrs. Even after extended duration of OER testing, the morphology of the reported NPLs was moderately retained. The reason behind this morphology change was

not associated with the transformation of catalyst but the presence of other entities in the sample. As mentioned in the preparation of working electrode section (see the Experimental section in the SI), that prior to OER test the catalyst was ultra-sonicated with carbon black and nafion in the presence of ethanol. The reported TEM analysis was conducted on the sample collected from the electrode after OER test. The presence of large molecule, such as Nafion, significantly hinders in getting high quality TEM images. To strengthen the claim of compositional retention, XPS analysis was conducted on Au-NiCoFe_7S_8 NPLs before and after OER measurements. The survey XPS spectra further supports the existence of all constituents before and after OER measurements. It should be noted here that the sharp fluorine (F) peak in survey XPS (Figure 6b1) was attributed to the Nafion used for the catalyst ink preparation. After OER, it is very critical to determine if the metal sulfides remained stable or got converted into oxides. The XPS analysis, Figure 6b1-b3, confirms the existence of S_{2p} assigned to S $2p_{3/2}$ and S $2p_{1/2}$ before and after OER (Figure 6b2-b3). This claim was supported by O 1s XPS (Figure S22) where before OER, O existed in the form physically adsorbed H_2O and OH^-. After 12 hrs of OER test, the shoulder peak at ~533 eV to sulphate (SO_4^{-2})[53] was observed which could be a result of sulfide dissolution after prolonged testing. To further demonstrate the preservation of compositional domains, Raman investigation was conducted on Au-NiCoFe_7S_8 NPLs. From Figure S23, the constancy of Raman stretching before and after OER test is quite evident. From these results, it is evident that the reported NPLs have good durability and resilience in OER experiment.[7, 8] It is important to note that apart mixed-valence characters Fe in Fe_7S_8 and dopants (Ni and Co) as shown in Figure 4, could dramatically restrict the tendency of the oxidation of NPLs during the OER process due to their rich surface dangling bonds and enhanced electron transfers, which offers exceptional stability to NPLs[37]. From these results, it is evident that the reported NPLs have good durability and resilience in OER experiment.

To provide further insights into the exceptionally high OER activity of co-doped Au-Fe_7S_8 NPLs, in particular to understand the critical roles of Co^{2+} and Ni^{2+} dopants in improving the

catalytic performance of Au-Fe_7S_8 NPLs, we employed the first-principal method to evaluate the catalytic properties of the doped Au-Fe_7S_8 NPLs (see the experimental section for details). OER process needs to complete four electron transfers, and generates *OH, *O, *OOH, and O_2 in the corresponding four elementary steps. OER energies drived by DFT calcuations (Figure 7a) alongside the (001) surface structures of Fe_7S_8 (Figure 7b-c) and configurations of adsorbed redox species on the pristine, Ni-doped and Co-doped Fe_7S_8 (001) surfaces (Figure 7d-l) were illustrated in Figure 7. Since the most exposed surfaces of Fe_7S_8 nanoplatelets are the {001} facets, we calculated the OER free energy barriers of the (001) surface for pristine, Ni- and Co-doped Fe_7S_8, as shown in Figure 7b. There are six adsorption sites on the pristine Fe_7S_8 (001) surface in our employed model (Figure 7c), and we have explored all possibilities. For the pristine surface, the most efficient site for OER is the Fe-S3 (Figure 7c). The limiting step is ΔG_3=1.87 V, which leads to an overpotential of 0.64 V. For both Ni- and Co-doped Fe_7S_8 (001), we have tested different surface sites by placing one dopant atom on either the surface layer or the sub-surface layer. The obtained most efficient site is still the Fe-S3 for both Ni- and Co-doped Fe_7S_8 (001). Both Ni and Co doped (001) can effectively lower the Gibbs free energy of step 3 (ΔG_3), leading to a drop of overpotential by ~50%. This is due to the improved binding of OOH species by Ni/Co doping. The overpotentials for Ni-, Co-, and Ni/Co doped Fe_7S_8 (001) NPLs derived by DFT calculations are consistent with the experimental values.

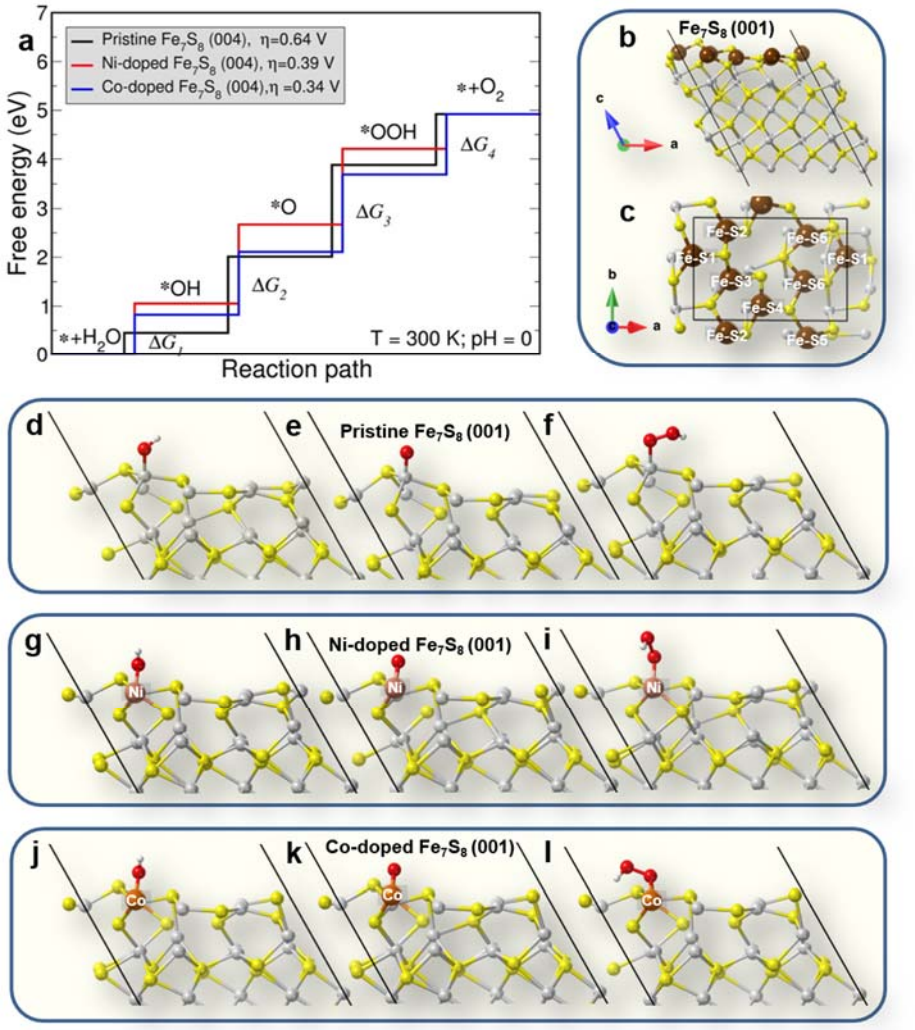

Figure 7. OER free energies calculated by DFT. (a) Plot of the 4-step Gibbs free energies calculated on the pristine, Ni-doped and Co-doped Fe_7S_8 (001) surfaces. (b and c) (001) surface structure of Fe_7S_8. Grey balls and yellows balls indicate Fe and S atoms, respectively, and brown balls indicate Fe atoms on the top layer. (d-l) Configurations of adsorbed redox species on the pristine, Ni-doped and Co-doped Fe_7S_8 (001) surfaces.

3. Conclusion

In summary, we have demonstrated the ability to build a collection of high order 2D heterostructures by a single-step ion diffusion of Ni and Co into the pristine Au-Fe_7S_8 NPLs to produce Au-$CoFe_7S_8$, Au-$NiFe_7S_8$ and Au-$NiCoFe_7S_8$. This simple alternative pathway, doping through ion diffusion, provides a straightforward opportunity to pre-program and rationally transform nanostructures into its derivatives which are otherwise inaccessible, while retaining

the morphology. The synthesized NPLs, Au-$NiCoFe_7S_8$, demonstrated exceptionally high OER performance with a lowest overpotential of 243 mV to attain the current density of 10 $mAcm^{-2}$ along with the Tafel slope of 43 $mVdec^{-1}$. The improved OER response of Ni and Co doped NPLs was attributed to the improved binding of OOH species on the (001) surfaces of Au-Fe_7S_8 NPLs by Ni/Co doping into the otherwise poor OER catalyst, i.e., pristine Au-Fe_7S_8 NPLs. Thus, the doping strategy demonstrated in this work can open new avenues for the development of efficient OER catalysts.

4. Experimental Section/Methods

Materials

Nickel (II) chloride hexahydrate ($NiCl_2.6H_2O$) (≥97%), cobalt (II) chloride hexahydrate ($CoCl_2.6H_2O$) (≥97%), hexadecylamine (HDA) (98%), sulfur (S) (99.99%) and oleylamine (OLA) (70%) were purchased from Sigma Aldrich. All chem2icals were used as received without further purification.

Synthesis of Au-Fe_7S_8 NPLs

The hybrid heterodimer of Au-Fe_7S_8 NPLs were synthesized with referring to the method developed by our group[45] with some modifications where thiol capped Au NPs were used as a seed for the consequent growth of Fe_7S_8 yielding Au-Fe_7S_8 NPLs.

Synthesis of Au-$CoFe_7S_8$ NPLs

The doping of Co and Ni metals into the pre-made Au-Fe_7S_8 hybrid NPLs [45] was performed by adding Co and Ni salts in the solution of pre-synthesized Au-Fe_7S_8 hybrid NPLs through ion diffusion.[34] For the synthesis of hexagonal shaped Au-$CoFe_7S_8$ NPLs, 0.0143 g of $CoCl_2.6H_2O$, 0.00048 g of HDA, 0.0048 g of S, 40 mg of Au-Fe_7S_8 dispersed in 1 ml of hexane and 7.5 ml of OLA were added in a 50 ml three-necked round bottom flask under continuous stirring. The reaction mixture was briefly purged with vacuum and refilled with N_2 three times at 80 °C to get rid of the hexane. The temperature of the reaction mixture was then gradually ramped up to 200 °C under inert atmosphere (N_2) and was left at this temperature for 3 hrs before removing

the heating mantle and allowing it to cool down to room temperature (RT). Ethanol was used to precipitate the NCs which were then centrifuged at 4500 rpm for 3 mins followed by re-dispersion in hexane containing 1% oleic acid (OA) and OLA.

Synthesis of Au-$NiFe_7S_8$ NPLs

The synthesis procedure of Au-$NiFe_7S_8$ was similar to the synthesis of Au-$CoFe_7S_8$, except that 0.0147 g of $NiCl_2.6H_2O$ was used rather than $CoCl_2.6H_2O$.

Synthesis of Au-$NiCoFe_7S_8$ NPLs

The synthesis procedure of Au-$NiCoFe_7S_8$ was similar to the synthesis of Au-$CoFe_7S_8$, except that both 0.0071g of $CoCl_2.6H_2O$ and 0.0073 g of $NiCl_2.6\ H_2O$ were used.

Preparation of working electrodes

Prior to the electrochemical measurements, the as-synthesized solids were calcined (to get rid of the surface ligands) under N_2 atmosphere at 430 °C for 1.5 h with a heating rate of 10 °C min^{-1}. 5 mg of the obtained catalyst powder was mixed with 3 mg of Super P® carbon black (Alfa Aesar) before suspending in 450 µL of absolute ethanol and 50 µL of 5 wt% Nafion® 117 solution (Sigma-Aldrich). The final suspension was sonicated for 1 h to produce a homogeneous ink. To prepare a glassy carbon (GC) electrode (0.196 cm^2) loaded catalyst sample, 5 µL of the as-prepared suspension was drop cast on it with a mass loading of ~0.255 mg cm^{-2} and left to dry under ambient conditions. In parallel, 100 µL of the suspension was drop cast on a 1cm×1cm carbon paper (Sigracet 39 AA, Fuel Cell Store), achieving a total catalyst mass of ~1 mg. The GC loaded RuO_2 sample was prepared by the same procedures using commercial RuO_2 powders purchased from Sigma-Aldrich (99.9% purity).

Characterization

The X-ray diffraction (XRD) patterns were acquired on D8 Advance powder diffractometer (Bruker AXS, Germany) with Cu Kα radiation (λ = 1.54Å) source at 40 KV/40 mA with a LynxEye detector. Transmission electron microscopy (TEM), high resolution TEM (HRTEM), high angle annular dark field-scanning TEM (HAADF-STEM), elemental mapping images,

energy dispersive X-ray spectroscopy (EDS), selected area electron diffraction (SAED) and fast Fourier transform (FFT) patterns were obtained on a FEI Talos F200X FEG-TEM with super-X EDS system (Thermo Fisher Scientific, Czech Republic) at John de Laeter Centre, Curtin University. X-ray photoelectron spectroscopy (XPS) measurements were collected on a Kratos AXIS Ultra DLD (Kratos Analytical, Manchester UK) at the John de Laeter Centre, Curtin University. For all samples, the binding energy was calibrated by setting the C 1s spectrum to the value of 284.8 eV. High resolution spectra were fitted with Gaussian-Lorentzian (70-30%) shape *via* linear background.

DFT calculations

Density functional calculations were performed by using the Vienna Ab initio Simulations Package (VASP)[73] and projected augmented wave (PAW) method (with $1s^1$, $2s^22p^4$, $3s^23p^4$, $3d^74s^1$, $3d^84s^2$ and $3d^84s^1$ as valence electrons for H, O, S, Fe, Ni and Co, respectively). The exchange-correlation interaction was treated with the generalized gradient approximation (GGA) in the Perdew, Burke and Ernzerhof (PBE)[74] parameterization. We employed GGA+U (U=3 and J=1)[37] to correct the self-interaction and over-delocalized *d* states. The monoclinic Fe_7S_8 (space group C2/c, No. 15) structure was fully relaxed by using GGA+U, and the energy was converged within 10^{-6} eV/cell and the force was converged to less than 10^{-2} eV/Å, with the cut-off energy of plane-wave basis set as 400 eV and a Gamma-centred k-point set of 2×4×2. The same cut-off energy and similar dense k-point set were used for slab calculations, except that only one k-point was used for the direction normal to the surface. A vacuum spacing no less than 15 Å was used in all slab calculations. The study of OER was then performed on the (001) surface. Gibbs free energy changes for the four elementary steps of OER were calculated following procedures detailed in previous publication.[75]

Declaration of competing interest

There are no conflicts to declare.

Acknowledgements

S.J. and X.X. contributed equally to this work. This work was supported by the Australian Research Council (ARC) Future Fellowship Scheme (G.J., FT210100509), the National Natural Science Foundation of China (No. 51675322), the Research Grants Council of Hong Kong (9048121), City University of Hong Kong (SRG 7005460), and Shenzhen Science Technology and Innovation Commission (R-IND12302). S.J. would like to especially thank Curtin strategic international research scholarship (CSIRS). This research was undertaken by using the facilities (TEM, XRD and XPS) at the John de Laeter Centre, Curtin University. The authors also acknowledge the use of equipment, scientific and technical assistance of the WA X-ray Surface Analysis Facility, funded by the Australian Research Council LIEF grant LE120100026.

Appendix A. Supplementary data

Supplementary data to this article can be found online.

References

[1] a) B. Zhang, X. Zheng, O. Voznyy, R. Comin, M. Bajdich, M. García-Melchor, L. Han, J. Xu, M. Liu, L. Zheng, F. P. G. De Arquer, C. T. Dinh, F. Fan, M. Yuan, E. Yassitepe, N. Chen, T. Regier, P. Liu, Y. Li, P. De Luna, A. Janmohamed, H. L. Xin, H. Yang, A. Vojvodic, E. H. Sargent, Homogeneously dispersed multimetal oxygen-evolving catalysts, Science 352 (2016) 333; b) X. Xu, W. Wang, W. Zhou, Z. Shao, Recent Advances in Novel Nanostructuring Methods of Perovskite Electrocatalysts for Energy-Related Applications, Small Methods 2 (2018) 1800071; c) J. Xia, H. Zhao, B. Huang, L. Xu, M. Luo, J. Wang, F. Luo, Y. Du, C.-H. Yan, Efficient Optimization of Electron/Oxygen Pathway by Constructing Ceria/Hydroxide Interface for Highly Active Oxygen Evolution Reaction, Adv. Funct. Mater. 30 (2020) 1908367; d) Y. Zhu, H. A. Tahini, Z. Hu, Z.-G. Chen, W. Zhou, A. C. Komarek, Q. Lin, H.-J. Lin, C.-T. Chen, Y. Zhong, M. T. Fernández-Díaz, S. C. Smith, H. Wang, M. Liu, Z. Shao,

Boosting Oxygen Evolution Reaction by Creating Both Metal Ion and Lattice-Oxygen Active Sites in a Complex Oxide, Adv. Mater. 32 (2020) 1905025.

[2] a) Z. W. Seh, J. Kibsgaard, C. F. Dickens, I. Chorkendorff, J. K. Nørskov, T. F. Jaramillo, Combining theory and experiment in electrocatalysis: Insights into materials design, Science 355 (2017) 4998. b) C. Bhattacharya, S. E. Saji, A. Mohan, V. Madav, G. Jia, Z. Yin, Sustainable Nanoplasmon-Enhanced Photoredox Reactions: Synthesis, Characterization, and Applications, Adv. Energy Mater. 10 (2020) 2002402; c) Y. Pang, N. Uddin, W. Chen, S. Javaid, E. Barker, Y. Li, A. Suvorova, M. Saunders, Z. Yin, G. Jia, Colloidal Single-Layer Photocatalysts for Methanol-Storable Solar H_2 Fuel, Adv. Mater. 31 (2019) 1905540.

[3] a) H. Sun, X. Xu, Y. Song, W. Zhou, Z. Shao, Designing High-Valence Metal Sites for Electrochemical Water Splitting, Adv. Funct. Mater. 31 (2021) 2009779; b) A. Grimaud, O. Diaz-Morales, B. Han, W. T. Hong, Y.-L. Lee, L. Giordano, K. A. Stoerzinger, M. T. M. Koper, Y. Shao-Horn, Activating lattice oxygen redox reactions in metal oxides to catalyse oxygen evolution, Nat. Chem. 9 (2017) 457; c) X. Zhu, T. Jin, C. Tian, C. Lu, X. Liu, M. Zeng, X. Zhuang, S. Yang, L. He, H. Liu, S. Dai, In Situ Coupling Strategy for the Preparation of FeCo Alloys and Co_4N Hybrid for Highly Efficient Oxygen Evolution, Adv. Mater. 29 (2017) 1704091; d) X. Xu, Y. Pan, L. Ge, Y. Chen, X. Mao, D. Guan, M. Li, Y. Zhong, Z. Hu, V. K. Peterson, M. Saunders, C.-T. Chen, H. Zhang, R. Ran, A. Du, H. Wang, S. P. Jiang, W. Zhou, Z. Shao, High-Performance Perovskite Composite Electrocatalysts Enabled by Controllable Interface Engineering, Small (2021) DOI: 10.1002/smll.202101573.

[4] a) N.-T. Suen, S.-F. Hung, Q. Quan, N. Zhang, Y.-J. Xu, H. M. Chen, Electrocatalysis for the oxygen evolution reaction: recent development and future perspectives, Chem Soc. Rev. 46 (2017) 337; b) Z. Lu, G. Neupane, Y. Du, D. Qi, Y. Lu, G. Jia, Z. Yin, 2D Materials Based on Main Group Element Compounds: Phases, Synthesis, Characterization, and Applications, Adv. Funct. Mater. 30 (2020) 2001127; c) Q. Hao, G. Jia, W. Wei, A. Vinu, Y. Wang, H. Arandiyan, B. Ni, Graphitic carbon nitride with different dimensionalities for energy and environmental

applications, Nano Res. 13 (2020) 18; d) N. Uddin, H. Zhang, Y. Du, G. Jia, S. Wang, Z. Yin, Structural-Phase Catalytic Redox Reactions in Energy and Environmental Applications, Adv. Mater. 32 (2020) 1905739.

[5] J. Wang, H. C. Zeng, CoHPi Nanoflakes for Enhanced Oxygen Evolution Reaction, ACS Appl. Mater. Interfaces. 10 (2018) 6288.

[6] T. Reier, M. Oezaslan, P. Strasser, Electrocatalytic Oxygen Evolution Reaction (OER) on Ru, Ir, and Pt Catalysts: A Comparative Study of Nanoparticles and Bulk Materials, ACS Catal. 2 (2012) 1765.

[7] Y. Pan, X. Xu, Y. Zhong, L. Ge, Y. Chen, J.-P. M. Veder, D. Guan, R. O'Hayre, M. Li, G. Wang, H. Wang, W. Zhou, Z. Shao, Direct evidence of boosted oxygen evolution over perovskite by enhanced lattice oxygen participation, Nat. Commun. 11 (2020) 2002.

[8] T. Kinner, K. P. Bhandari, E. Bastola, B. M. Monahan, N. O. Haugen, P. J. Roland, T. P. Bigioni, R. J. Ellingson, Majority Carrier Type Control of Cobalt Iron Sulfide ($Co_xFe_{1-x}S_2$) Pyrite Nanocrystals, J. Phys. Chem. C 120 (2016) 5706.

[9] M. Shen, C. Ruan, Y. Chen, C. Jiang, K. Ai, L. Lu, Covalent Entrapment of Cobalt–Iron Sulfides in N-Doped Mesoporous Carbon: Extraordinary Bifunctional Electrocatalysts for Oxygen Reduction and Evolution Reactions, ACS Appl. Mater. Interfaces 7 (2015) 207.

[10] X. Xia, C. Zhu, J. Luo, Z. Zeng, C. Guan, C. F. Ng, H. Zhang, H. J. Fan, Synthesis of free-standing metal sulfide nanoarrays via anion exchange reaction and their electrochemical energy storage application, Small 10 (2014) 766.

[11] Z. Peng, D. Jia, A. M. Al-Enizi, A. A. Elzatahry, G. Zheng, Electrocatalysts: From Water Oxidation to Reduction: Homologous Ni–Co Based Nanowires as Complementary Water Splitting Electrocatalysts, Adv. Energy Mater. 5 (2015) 1402031.

[12] X. Xu, C. Su, W. Zhou, Y. Zhu, Y. Chen, Z. Shao, Co-doping Strategy for Developing Perovskite Oxides as Highly Efficient Electrocatalysts for Oxygen Evolution Reaction, Adv. Sci. 3 (2016) 1500187.

[13] S. Jin, Are Metal Chalcogenides, Nitrides, and Phosphides Oxygen Evolution Catalysts or Bifunctional Catalysts?, ACS Energy Lett. 2 (2017) 1937.

[14] B. Zhang, X. Zheng, O. Voznyy, R. Comin, M. Bajdich, M. García-Melchor, L. Han, J. Xu,1 M. Liu, L. Zheng, F. P. García de Arquer, C. T. Dinh, F. Fan, M. Yuan, E. Yassitepe, N. Chen, T. Regier, P. Liu, Y. Li, P. De Luna, A. Janmohamed, H. L. Xin, H. Yang, A. Vojvodic, E. H. Sargent, Homogeneously dispersed multimetal oxygen-evolving catalysts, Science 352 (2016), 333.

[15] J. Zhang, Y. Zhao, X. Guo, C. Chen, C.-L. Dong, R.-S. Liu, C.-P. Han, Y. Li, Y. Gogotsi, G. Wang, Single platinum atoms immobilized on an MXene as an efficient catalyst for the hydrogen evolution reaction, Nat. Catal. 3 (2020) 985.

[16] C. Xia, Q. Jiang, C. Zhao, M. N. Hedhili, H. N. Alshareef, Selenide-Based Electrocatalysts and Scaffolds for Water Oxidation Applications, Adv. Mater. 28 (2016) 77.

[17] P. Ganesan, M. Prabu, J. Sanetuntikul, S. Shanmugam, Cobalt Sulfide Nanoparticles Grown on Nitrogen and Sulfur Codoped Graphene Oxide: An Efficient Electrocatalyst for Oxygen Reduction and Evolution Reactions, ACS Catal. 5 (2015) 3625.

[18] C. Tang, A.M. Asiri, X. Sun, Highly-active oxygen evolution electrocatalyzed by a Fe-doped NiSe nanoflake array electrode, Chem. Commun., 52 (2016) 4529.

[19] X.-Y. Yu, Y. Feng, B. Guan, X. W. Lou, U. Paik, Carbon coated porous nickel phosphides nanoplates for highly efficient oxygen evolution reaction, Energy Environ. Sci. 9 (2016) 1246.

[20] X.-Y. Yu, X.W. Lou, Mixed Metal Sulfides for Electrochemical Energy Storage and Conversion, Adv. Energy Mater. 8 (2018) 1701592.

[21] G. Fu, J.-M. Lee, Ternary metal sulfides for electrocatalytic energy conversion, J. Mater. Chem. A 7 (2019) 9386.

[22] J. Yang, G. Zhu, Y. Liu, J. Xia, Z. Ji, X. Shen, S. Wu, Fe_3O_4-Decorated Co_9S_8 Nanoparticles In Situ Grown on Reduced Graphene Oxide: A New and Efficient Electrocatalyst for Oxygen Evolution Reaction, Adv. Funct. Mater. 26 (2016) 4712.

[23] K. Zhan, C. Feng, X. Feng, D. Zhao, S. Yue, Y. Li, Q. Jiao, H. Li, Y. Zhao, Iron-Doped Nickel Cobalt Phosphide Nanoarrays with Urchin-like Structures as High-Performance Electrocatalysts for Oxygen Evolution Reaction, ACS Sustainable Chem. Eng. 8 (2020) 6273.

[24] B.-Q. Li, S.-Y. Zhang, C. Tang, X. Cui, Q. Zhang, Anionic Regulated NiFe (Oxy)Sulfide Electrocatalysts for Water Oxidation, Small 13 (2017) 1700610.

[25] L. Huang, H. Wu, H. Liu, Y. Zhang, Phosphorous doped cobalt-iron sulfide/carbon nanotube as active and robust electrocatalysts for water splitting, Electrochim. Acta 318 (2019) 892.

[26] C. Liu, D. Jia, Q. Hao, X. Zheng, Y. Li, C. Tang, H. Liu, J. Zhang, X. Zheng, P-Doped Iron-Nickel Sulfide Nanosheet Arrays for Highly Efficient Overall Water Splitting, ACS Appl. Mater. Interfaces 11 (2019) 27667.

[27] D. Li, H. Liu, L. Feng, A Review on Advanced FeNi-Based Catalysts for Water Splitting Reaction, Energy Fuels 34 (2020) 13491.

[28] J. M. Rhodes, J. R. McBride, J. E. Macdonald, Synthesis of FeS_2–CoS_2 Core–Frame and Core–Shell Hybrid Nanocubes, Chem. Mater. 30 (2018) 8121.

[29] J. Yu, G. Cheng, W. Luo, Ternary nickel–iron sulfide microflowers as a robust electrocatalyst for bifunctional water splitting, J. Mater. Chem. A 5 (2017) 15838.

[30] A. L. Abdelhady, M. A. Malik, P. O'Brien, F. Tuna, Nickel and Iron Sulfide Nanoparticles from Thiobiurets, J. Phys. Chem. C 116 (2012) 2253.

[31] X. Long, G. Li, Z. Wang, H. Zhu, T. Zhang, S. Xiao, W. Guo, S. Yang, Metallic Iron–Nickel Sulfide Ultrathin Nanosheets As a Highly Active Electrocatalyst for Hydrogen Evolution Reaction in Acidic Media, J. Am. Chem. Soc. 137 (2015) 11900.

[32] R. Buonsanti, D. J. Milliron, Chemistry of Doped Colloidal Nanocrystals, Chem. Mater. 25 (2013) 1305.

[33] D. Chen, R. Viswanatha, G. L. Ong, R. Xie, M. Balasubramanian, X. Peng, Temperature Dependence of "Elementary Processes" in Doping Semiconductor Nanocrystals, J. Am. Chem. Soc. 131 (2009) 9333.

[34] D. Mocatta, G. Cohen, J. Schattner, O. Millo, E. Rabani, U. Banin, Heavily Doped Semiconductor Nanocrystal Quantum Dots, Science 332 (2011) 77.

[35] W. Zhu, Z. Yue, W. Zhang, N. Hu, Z. Luo, M. Ren, Z. Xu, Z. Wei, Y. Suo, J. Wang, Wet-chemistry topotactic synthesis of bimetallic iron–nickel sulfide nanoarrays: an advanced and versatile catalyst for energy efficient overall water and urea electrolysis, J. Mater. Chem. A 6 (2018) 4346.

[36] Y. Zhou, M. Luo, Z. Zhang, W. Li, X. Shen, W. Xia, M. Zhou, X. Zeng, Iron doped cobalt sulfide derived boosted electrocatalyst for water oxidation, Appl. Surf. Sci. 448 (2018) 9.

[37] S. Chen, Z. Kang, X. Zhang, J. Xie, H. Wang, W. Shao, X. Zheng, W. Yan, B. Pan, Y. Xie, Highly Active Fe Sites in Ultrathin Pyrrhotite Fe_7S_8 Nanosheets Realizing Efficient Electrocatalytic Oxygen Evolution, ACS Cent. Sci. 3 (2017) 1221.

[38] C. Feng, M. B. Faheem, J. Fu, Y. Xiao, C. Li, Y. Li, Fe-Based Electrocatalysts for Oxygen Evolution Reaction: Progress and Perspectives, ACS Catal. 10 (2020) 4019.

[39] U. Becker, A. W. Munz, A. R. Lennie, G. Thornton, D. J. Vaughan, The atomic and electronic structure of the (001) surface of monoclinic pyrrhotite (Fe7S8) as studied using STM, LEED and quantum mechanical calculations, Surf. Sci. 389 (1997) 66.

[40] S. Javaid, X. Li, F. Wang, W. Chen, Y. Pang, S. Wang, G. Jia, F. Jones, Synthesis of magnetically separable Fe_3O_4–Au–CdS kinked heterotrimers incorporating plasmonic and semiconducting functionalities, J. Mater. Chem. C 7 (2019) 14517.

[41] J. Landon, E. Demeter, N. İnoğlu, C. Keturakis, I. E. Wachs, R. Vasić, A. I. Frenkel, J. R. Kitchin, Spectroscopic Characterization of Mixed Fe–Ni Oxide Electrocatalysts for the Oxygen Evolution Reaction in Alkaline Electrolytes, ACS Catal. 2 (2012) 1793.

[42] S.-F. Hung, Y.-Y. Hsu, C.-J. Chang, C.-S. Hsu, N.-T. Suen, T.-S. Chan, H. M. Chen, Unraveling Geometrical Site Confinement in Highly Efficient Iron-Doped Electrocatalysts toward Oxygen Evolution Reaction, Adv. Energy Mater. 8 (2018) 1701686.

[43] L. Calvillo, F. Carraro, O. Vozniuk, V. Celorrio, L. Nodari, A. E. Russel, D. Debellis, D. Fermin, F. Cavani, S. Agnoli, G. Granozzi, Insights into the durability of Co–Fe spinel oxygen evolution electrocatalysts via operando studies of the catalyst structure, J. Mater. Chem. A 6 (2018) 7034.

[44] A. Riedinger, F. D. Ott, A. Mule, S. Mazzotti, P. N. Knüsel, S. J. P. Kress, F. Prins, S. C. Erwin, D. J. Norris, An intrinsic growth instability in isotropic materials leads to quasi-two-dimensional nanoplatelets, Nat. Mater. 16 (2017) 743.

[45] S. Javaid, Y. Li, D. Chen, X. Xu, Y. Pang, W. Chen, F. Wang, Z. Shao, M. Saunders, J.-P. Veder, G. Jia, F. Jones, Spontaneous Formation of Heterodimer Au–Fe_7S_8 Nanoplatelets by a Seeded Growth Approach, J. Phys. Chem. C 123 (2019) 10604.

[46] D. Barman, S. Ghosh, S. Paul, B. Dalal, S. K. De, Cation Exchange-Mediated Synthesis of Library of Plasmomagnetic Nanoheterostructures: Transformation of 2-Dimensional-Shaped Fe7S8 Nanoplates to Cu–Fe–S-Based Ternary Compound, Chem. Mater. 30 (2018) 5550.

[47] Y. Zhang, Y. Du, H. Xu, Q. Wang, Diverse-shaped iron sulfidenanostructures synthesized from a single source precursor approach, CrystEngComm 12 (2010) 12 3658.

[48] W. Han, M. Gao, Cryst. Investigations on Iron Sulfide Nanosheets Prepared via a Single-Source Precursor Approach, Growth Des. 8 (2008) 1023.

[49] G. He, M. Qiao, W. Li, Y. Lu, T. Zhao, R. Zou, B. Li, J. A. Darr, J. Hu, M.-M. Titirici, I. P. Parkin, S, N-Co-Doped Graphene-Nickel Cobalt Sulfide Aerogel: Improved Energy Storage and Electrocatalytic Performance, Adv. Sci. 4 (2017) 1600214.

[50] X. Liu, W. Zang, C. Guan, L. Zhang, Y. Qian, A. M. Elshahawy, D. Zhao, S. J. Pennycook, J. Wang, Ni-Doped Cobalt–Cobalt Nitride Heterostructure Arrays for High-Power Supercapacitors, ACS Energy Lett. 3 (2018) 2462.

[51] Q. Li, X. Wang, K. Tang, M. Wang, C. Wang, C. Yan, Electronic Modulation of Electrocatalytically Active Center of Cu7S4 Nanodisks by Cobalt-Doping for Highly Efficient Oxygen Evolution Reaction, ACS Nano 11 (2017) 12230.

[52] W. Wei, L. Mi, Y. Gao, Z. Zheng, W. Chen, X. Guan, Partial Ion-Exchange of Nickel-Sulfide-Derived Electrodes for High Performance Supercapacitors, Chem. Mater. 26 (2014) 3418.

[53] A. Ghahremaninezhad, D. G. Dixon, E. Asselin, Electrochemical and XPS analysis of chalcopyrite (CuFeS2) dissolution in sulfuric acid solution, ElectroChim. Acta 87 (2013) 97.

[54] C. Nims, B. Cron, M. Wetherington, J. Macalady, J. Cosmidis, Low frequency Raman Spectroscopy for micron-scale and in vivo characterization of elemental sulfur in microbial samples, Sci. Rep. 9 (2019) 7971.

[55] R. Bolagam, S. Um, Hydrothermal Synthesis of Cobalt Ruthenium Sulfides as Promising Pseudocapacitor Electrode Materials. Coat. 10 (2020) 200.

[56] Z. Cheng, H. Abernathy, M. Liu, Raman Spectroscopy of Nickel Sulfide Ni_3S_2, J. Phys. Chem. C 111 (2007) 17997.

[57] Y. Guo, J. Tang, H. Qian, Z. Wang, Y. Yamauchi, One-Pot Synthesis of Zeolitic Imidazolate Framework 67-Derived Hollow Co_3S_4@MoS_2 Heterostructures as Efficient Bifunctional Catalysts, Chem. Mater. 29 (2017) 5566.

[58] M. Chauhan, K. P. Reddy, C. S. Gopinath, S. Deka, Copper Cobalt Sulfide Nanosheets Realizing a Promising Electrocatalytic Oxygen Evolution Reaction, ACS Catal. 7 (2017) 5871.

[59] P. Cai, J. Huang, J. Chen, Z. Wen, Oxygen-Containing Amorphous Cobalt Sulfide Porous Nanocubes as High-Activity Electrocatalysts for the Oxygen Evolution Reaction in an Alkaline/Neutral Medium, Angew. Chem. Int. Ed. 56 (2017) 4858.

[60] J. Zhou, Y. Dou, A. Zhou, R.-M. Guo, M.-J. Zhao, J.-R. Li, MOF Template-Directed Fabrication of Hierarchically Structured Electrocatalysts for Efficient Oxygen Evolution Reaction, Adv. Energy Mater. 7 (2017) 1602643.

[61] H. Xu, J. Cao, C. Shan, B. Wang, P. Xi, W. Liu, Y. Tang, MOF-Derived Hollow CoS Decorated with CeOx Nanoparticles for Boosting Oxygen Evolution Reaction Electrocatalysis, Angew. Chem. Int. Ed. 57 (2018) 8654.

[62] H. Han, K. M. Kim, H. Choi, G. Ali, K. Y. Chung, Y.-R, Hong, J. Choi, J. Kwon, S. W. Lee, J. W. Lee, J. H. Ryu, T. Song, S. Mhin, Parallelized Reaction Pathway and Stronger Internal Band Bending by Partial Oxidation of Metal Sulfide–Graphene Composites: Important Factors of Synergistic Oxygen Evolution Reaction Enhancement, ACS Catal. 8 (2018) 4091.

[63] J. Wang, W. Yang, J. Liu, CoP_2 nanoparticles on reduced graphene oxide sheets as a super-efficient bifunctional electrocatalyst for full water splitting, J. Mater. Chem. A, 4 (2016) 4686.

[64] S. Yang, G. Chen, A. G. Ricciardulli, P. Zhang, Z. Zhang, H. Shi, J. Ma, J. Zhang, P. W. M. Blom, X. Feng, Topochemical Synthesis of Two-Dimensional Transition-Metal Phosphides Using Phosphorene Templates, Angew. Chem. Int. Ed. 59 (2020) 465.

[65] C. Xiao, X. Lu, C. Zhao, Unusual synergistic effects upon incorporation of Fe and/or Ni into mesoporous Co_3O_4 for enhanced oxygen evolution, Chem. Commun. 50 (2014) 10122.

[66] J. Bao, X. Zhang, B. Fan, J. Zhang, M. Zhou, W. Yang, X. Hu, H. Wang, B. Pan, Y. Xie, Ultrathin Spinel-Structured Nanosheets Rich in Oxygen Deficiencies for Enhanced Electrocatalytic Water Oxidation, Angew. Chem. Int. Ed. 54 (2015) 7399.

[67] F. Song, X. Hu, Ultrathin Cobalt–Manganese Layered Double Hydroxide Is an Efficient Oxygen Evolution Catalyst, J. Am. Chem. Soc. 136 (2014) 16481.

[68] J. Nai, H. Yin, T. You, L. Zheng, J. Zhang, P. Wang, Z. Jin, Y. Tian, J. Liu, Z. Tang, L. Guo, Efficient Electrocatalytic Water Oxidation by Using Amorphous Ni–Co Double Hydroxides Nanocages, Adv. Energy Mater. 5 (2015) 1401880.

[69] Y. Zhu, G. Chen, Y. Zhong, Y. Chen, N. Ma, W. Zhou, Z. Shao, A surface-modified antiperovskite as an electrocatalyst for water oxidation, Nat. Commun. 9 (2018) 2326.

[70] S. Zhao, R. Jin, H. Abroshan, C. Zeng, H. Zhang, S. D. House, E. Gottlieb, H. J. Kim, J. C. Yang, R. Jin, Gold Nanoclusters Promote Electrocatalytic Water Oxidation at the Nanocluster/CoSe2 Interface, J. Am. Chem. Soc. 139 (2017) 1077.

[71] Y. Gorlin, C.-J. Chung, J. D. Benck, D. Nordlund, L. Seitz, T.-C. Weng, D. Sokaras, B. M. Clemens, T. F. Jaramillo, Understanding Interactions between Manganese Oxide and Gold That Lead to Enhanced Activity for Electrocatalytic Water Oxidation, J. Am. Chem. Soc. 136 (2014) 4920.

[72] P. Rasiyah, A. C. C. Tseung, The Role of the Lower Metal Oxide/Higher Metal Oxide Couple in Oxygen Evolution Reactions, J. Electrochem Soc. 131 (1984) 803.

[73] G. Kresse, D. Joubert, From ultrasoft pseudopotentials to the projector augmented-wave method, Phys. Rev. B 59 (1999) 1758.

[74] J. P. Perdew, K. Burke, M. Ernzerhof, Generalized Gradient Approximation Made Simple, Phys. Rev. Lett. 77 (1996) 3865.

[75] D. Chen, H. Zhang, Y. Li, Y. Pang, Z. Yin, H. Sun, L.-C. Zhang, S. Wang, M. Saunders, E. Barker, G. Jia, Spontaneous Formation of Noble- and Heavy-Metal-Free Alloyed Semiconductor Quantum Rods for Efficient Photocatalysis, Adv. Mater. 30 (2018) 1803351.

Highlights:

- The ultrafast and single step ion diffusion method is developed to produce Ni and Co heavily doped 2D Au-Fe_7S_8 nanoplatelets.
- The unique cohabitation of Ni^{+2} and Co^{2+} with Fe_7S_8 transforms it from least to exceptionally high performing oxygen evolution reaction (OER) active material with an OER overpotential of 243 mV at 10 mA cm^{-2} and fast kinetics with Tafel slop of 43 mV dec^{-1}.
- Hexagonal morpholgoy and location of Au seed was retained in the pristine Au-Fe_7S_8 NPLs before and after OER testing.

Credit author statement:

Shaghraf Javaid: Synthesis of reported materials, characterization, writing original draft. Xiaomin Xu: Conducted OER experiments, writing and editing of the draft. Wei Chen, Jiayi Chen: Synthesis of reported materials, experimental data analysis. Hsien-Yi Hsu, Sheng Wang, Xuyong Yang: experimental data analysis. Yunguo Li, Zongping Shao, Franca Jones, Guohua Jia, : Conceived the idea and provided timely supervision and recommendations.

Shaghraf received her PhD degree in chemistry from Curtin University in 2019. Her research work was focused on the development of novel hybrid nanostructures. In 2019, she was also short-listed and eventually selected as the winner of “Future scientist Award”, in Western Australia (WA). Afterwards, she secured and completed a postdoc in 2020 on the development of electrochemical sensors. Currently, she is working as an electrochemist in a biomedical company for the development of foetal monitoring sensors.

Xiaomin Xu received his Ph.D. in Chemical Engineering from Curtin University, Australia. He is currently a Research Associate at Curtin University. His research interests are mainly focused on the development of perovskite oxides and other functional materials for applications in electrochemical energy storage and conversion.

Wei Chen received her Ph.D. in Chemistry from Curtin University, Australia. Her research interests are mainly focused on the synthesis of low-dimension nanomaterials and application in photochemical and electrochemical energy storage. She is currently a postdoctoral fellow in the Chinese Academy of Sciences.

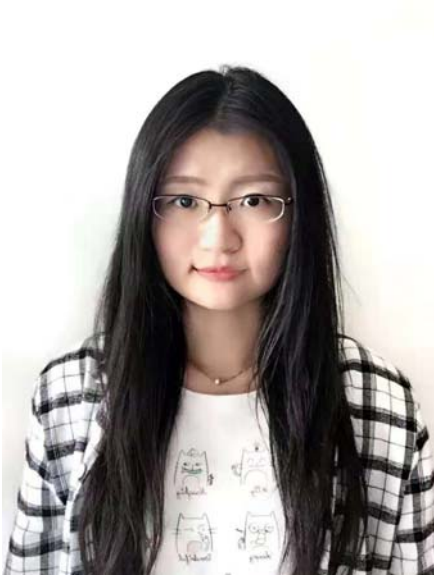

Jiayi Chen is a PhD student under the supervison of Dr. Guohua Jia at Curtin University. Her research focuses on the development of colloidal semiconductor nanocrystals for latent fingermark detection and photocatalytic applications.

Dr. Hsien-Yi (Sam) HSU is currently an Assistant Professor in the School of Energy and Environment at City University of Hong Kong. He obtained his PhD degree under supervision of Prof. Kirk S. SCHANZE at University of Florida with focusing on photophysical behaviors for solar energy applications. After that, he received the two-year postdoctoral and research associate's appointments respectively with Prof. Allen J. BARD and Prof. Edward T. YU at University of Texas at Austin. The area of his expertise stretches from material design to new related disciplines involving material characterization and diverse applications, such as electrocatalysis, photocatalysis, and photoelectrocatalysis.

Sheng Wang received his Ph.D. from Jilin University, China. He is currently a postdoctoral researcher at Shanghai University, China. His research interests are mainly focused on the synthesis of II-VI, III-V and perovskite nanocrystals and their applications in light-emitting diodes and amplified spontaneous emission.

Xuyong Yang is a Full Professor in Shanghai University, China. He received his PhD degree in microelectronics from Nanyang Technological University in Singapore in 2014, and worked as a postdoc at the same university prior to beginning his independent research career at Shanghai University. His research focuses primarily on design and fabrication of low dimensional semiconductor nanomaterials such as quantum dots and nanorods, as well as their applications in various optoelectronic devices.

Yunguo Li is a Research Professor at the School of Earth and Space Sciences, University of Science and Technology of China. He received his PhD degree at the Department of Materials Science and Engineering, Royal Institute of Technology, Sweden. He works in the area of computational materials science, mineral physics and geochemistry.

Zongping Shao is a John Curtin Distinguished Professor at Curtin University, Australia, and also a professor at Nanjing Tech University, China. He obtained his Ph.D. from Dalian Institute of Chemical Physics, China, in 2000. He worked as a Visiting Scholar at Institut de Researches Sur La Catalyse, CNRS, France, and then a Postdoctoral Fellow at California Institute of Technology, USA, from 2000 to 2005. His current research interests include fuel cells, lithium-ion batteries, metal-air batteries, solar cells, and oxygen-permeable membranes. He has been recognized as a Highly Cited Researcher by Clarivate Analytics since 2017.

Dr Franca Jones did her undergraduate degree at the University of Sydney (with honours) before completing her PhD studies at the then Curtin University of Technology in collaboration with the AJ Parker Cooperative Research Centre for Hydrometallurgy. After graduating she undertook a two-year postdoctoral stint at the Max Plank Institute for Colloids and Interfaces in Potsdam Germany before returning to Australia. She is currently at Curtin University and her research interests are in all aspects of crystallization.

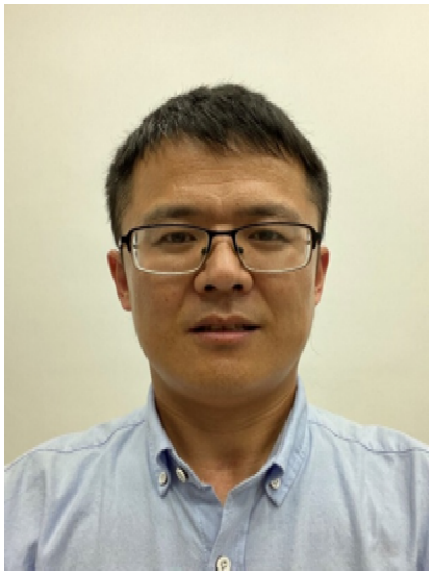

Guohua Jia is an ARC Future Fellow in the School of Molecular and Life Science at Curtin University, Australia. He obtained his PhD degree in chemistry in 2009 from City University of Hong Kong. He was a postdoctoral fellow at the Hebrew University of Jerusalem in Israel from 2010 to 2014 prior to his current appointment. His research interests focus on chemistry and physics of colloidal nanocrystals, with particular emphasis on their shape-dependent properties and applications in optoelectronic devices and catalysis.